The Astrophysical Journal, 780:31 (9pp), 2014 January 1 doi:10.1088/0004-637X/780/1/31

RADIOACTIVELY POWERED EMISSION FROM BLACK HOLE–NEUTRON STAR MERGERS

Masaomi Tanaka[1], Kenta Hotokezaka[2], Koutarou Kyutoku[3], Shinya Wanajo[1],
Kenta Kiuchi[4], Yuichiro Sekiguchi[4], and Masaru Shibata[4]
[1] National Astronomical Observatory of Japan, Mitaka, Tokyo 181-8588, Japan; masaomi.tanaka@nao.ac.jp
[2] Department of Physics, Kyoto University, Kyoto 606-8502, Japan
[3] Department of Physics, University of Wisconsin-Milwaukee, P.O. Box 413, Milwaukee, WI 53201, USA
[4] Yukawa Institute for Theoretical Physics, Kyoto University, Kyoto 606-8502, Japan
Received 2013 October 10; accepted 2013 November 5; published 2013 December 10

ABSTRACT

Detection of the electromagnetic counterparts of gravitational wave (GW) sources is important to unveil the nature of compact binary coalescences. We perform three-dimensional, time-dependent, multi-frequency radiative transfer simulations for radioactively powered emission from the ejecta of black hole (BH)–neutron star (NS) mergers. Depending on the BH to NS mass ratio, spin of the BH, and equations of state of dense matter, BH–NS mergers can eject more material than NS–NS mergers. In such cases, radioactively powered emission from the BH–NS merger ejecta can be more luminous than that from NS–NS mergers. We show that, in spite of the expected larger distances to BH–NS merger events, the observed brightness of BH–NS mergers can be comparable to or even higher than that of NS–NS mergers. We find that, when the tidally disrupted BH–NS merger ejecta are confined to a small solid angle, the emission from BH–NS merger ejecta tends to be bluer than that from NS–NS merger ejecta for a given total luminosity. Thanks to this property, we might be able to distinguish BH–NS merger events from NS–NS merger events by multi-band observations of the radioactively powered emission. In addition to the GW observations, such electromagnetic observations can potentially provide independent information on the progenitors of GW sources and the nature of compact binary coalescences.

Key words: gamma-ray burst: general – gravitational waves – nuclear reactions, nucleosynthesis, abundances – radiative transfer

Online-only material: color figures

1. INTRODUCTION

Next-generation gravitational wave (GW) detectors, such as Advanced LIGO, Advanced Virgo, and KAGRA (Abadie et al. 2010b; Kuroda & LCGT Collaboration 2010; Accadia et al. 2011; Aasi et al. 2013b), are expected to detect GW signals from compact binary coalescences. Mergers of a black hole (BH) and neutron star (NS) binary are among the promising sources of GWs (see Shibata & Taniguchi 2011 for a review). Although the BH–NS merger rate is estimated to be lower than the NS–NS merger rate by a factor of ∼10–100, the detection rates can be comparable thanks to expected larger horizon distances to the BH–NS mergers by a factor of about two. The expected detection rate of BH–NS mergers with the advanced detectors is ∼10 yr^{-1} (with the lower and upper estimation of 0.2 and 300 yr^{-1}, respectively; see Abadie et al. 2010a).

Even if GWs are detected by several detectors, the position of the GW source cannot be accurately determined (a typical localization is about 10–100 deg^2; e.g., Abadie et al. 2012; Aasi et al. 2013b). Therefore, to study the nature of the GW sources, identification of electromagnetic (EM) counterparts is crucial (Nissanke et al. 2013; Kelley et al. 2013; Kasliwal & Nissanke 2013, and see Aasi et al. 2013a for the first actual searches). Short gamma-ray bursts (GRBs) are promising candidates (Kochanek & Piran 1993), but the association fraction will not be large if the jet is beamed into a small solid angle. Motivated by these facts, possible isotropic EM signals from GW sources have been suggested (e.g., Li & Paczyński 1998; Metzger & Berger 2012; Kyutoku et al. 2012; Rosswog et al. 2013b; Piran et al. 2013; Takami et al. 2013).

The emission powered by the radioactive energy of *r*-process nuclei is one of the important targets for follow-up EM observations. For the case of NS–NS mergers, part of the material is expected to be ejected (e.g., Rosswog et al. 1999; Lee & Ramirez-Ruiz 2007; Goriely et al. 2011; Hotokezaka et al. 2013a; Bauswein et al. 2013), and *r*-process nucleosynthesis is thought to take place in the ejecta (e.g., Symbalisty & Schramm 1982; Eichler et al. 1989; Meyer 1989; Freiburghaus et al. 1999; Roberts et al. 2011; Goriely et al. 2011; Korobkin et al. 2012; Bauswein et al. 2013; Rosswog et al. 2013a). By the decay energy of the synthesized nuclei, the ejecta can emit ultraviolet–optical–infrared (UVOIR) radiation (Li & Paczyński 1998). This is a similar emission mechanism to supernovae, where ^{56}Ni is the dominant heating source. Such emission from NS–NS mergers has been called "kilonova," "macronova," or "mini-supernova" (Kulkarni 2005; Metzger et al. 2010; Roberts et al. 2011; Goriely et al. 2011; Metzger & Berger 2012).

Kasen et al. (2013), Barnes & Kasen (2013), and Tanaka & Hotokezaka (2013, hereafter TH13) performed radiative transfer simulations for radioactively powered emission from NS–NS mergers, taking into account the wavelength-dependent opacity of *r*-process elements. They found that (1) the luminosity is about 10^{41} erg s^{-1} (for the ejecta mass of $M_{\rm ej} = 10^{-2}\,M_\odot$), (2) the spectral energy distribution peaks at the red edge of optical and near-infrared (NIR) wavelengths, and (3) the emission lasts about 5–20 days. In fact, following the *Swift* detection of the short GRB 130603B (Melandri et al. 2013; see also de Ugarte Postigo et al. 2013), a bright NIR excess was detected in the afterglow (Berger et al. 2013; Tanvir et al. 2013). This NIR emission can be interpreted as radioactively powered emission, being broadly consistent with the results of radiative transfer

simulations (Berger et al. 2013; Tanvir et al. 2013; Hotokezaka et al. 2013b).[5] If this interpretation is the case, this discovery suggests that radioactively powered emission actually takes place in binary coalescences, and it could be used for the localization of GW sources.

Mass ejection and the *r*-process are also expected in BH–NS mergers (Lattimer & Schramm 1974, 1976). Depending on the BH to NS mass ratio, spin of the BH, and equations of state (EOSs) adopted in the merger simulations, BH–NS mergers can eject more material than NS–NS mergers (Rosswog 2005; Kyutoku et al. 2011, 2013; Foucart et al. 2013; Lovelace et al. 2013; Deaton et al. 2013). Kyutoku et al. (2013) also showed that the mass ejection can be highly asymmetric. They discussed the impacts of asymmetric mass ejection on the properties of the EM counterparts.

In this paper, we study the properties of radioactively powered emission from BH–NS mergers. We perform three-dimensional, time-dependent, multi-frequency radiative transfer simulations of the BH–NS merger ejecta for the first time. In Section 2, we describe our models of BH–NS mergers and simulation methods. The results of the radiative transfer simulations are shown in Section 3. Implications for EM observations following GW detection are discussed in Section 4. Finally, we give our conclusions in Section 5.

2. MODELS AND METHODS

2.1. Models

We use the results of numerical-relativity simulations by Kyutoku et al. (2013) as the input models of our radiative transfer simulations. We adopt three models with different EOSs. The adopted EOSs are APR4 (Akmal et al. 1998), H4 (Glendenning & Moszkowski 1991; Lackey et al. 2006), and MS1 (Müller & Serot 1996). APR4 is a "soft" EOS, giving a radius of 11.1 km for a 1.35 $M_\odot$ NS, while H4 and MS1 are "stiff" EOSs, giving radii of 13.6 km and 14.4 km for a 1.35 $M_\odot$ NS, respectively. For more details on these EOSs, see Hotokezaka et al. (2013a). For all of the models, the gravitational mass of the NS is fixed to be $M_{\rm NS} = 1.35\,M_\odot$. The mass ratio of BH to NS, $Q = M_{\rm BH}/M_{\rm NS}$, is set to be 3 ($M_{\rm BH} = 4.05\,M_\odot$). In all of the models, the non-dimensional spin parameter of the BH is set to be $\chi = 0.75$, with the direction aligned with the binary orbital angular momentum.

With this BH spin parameter, NSs are tidally disrupted by BHs with a wide range of mass ratios and EOSs. The ejecta masses ($M_{\rm ej}$) do not depend strongly on the mass ratios except for the soft EOSs, such as APR4. For the stiff EOSs H4 and MS1, the ejecta masses are not smaller than $10^{-2}\,M_\odot$, i.e., $M_{\rm ej} \sim$ (4–8) $\times\, 10^{-2}\,M_\odot$ (for Q = 3–7 and $\chi = 0.75$; Kyutoku et al. 2013; see also Table 1). For the soft EOS APR4, the ejecta mass decreases as the BH mass increases, from $M_{\rm ej} \sim 1 \times 10^{-2}\,M_\odot$ (for $Q = 3$) down to $M_{\rm ej} \sim 5 \times 10^{-4}\,M_\odot$ (for $Q = 7$; see Hotokezaka et al. 2013b). The mass ejection is also affected by the BH spin. When a non-spinning BH is considered, the ejecta mass can be substantially smaller than $10^{-2}\,M_\odot$ (K. Kyutoku et al., in preparation). In this paper, we focus on the three models with relatively efficient mass ejection.

As described by Li & Paczyński (1998), the behavior of radioactively powered emission is mainly determined by the mass of the ejecta and the characteristic velocity ($v_{\rm ch} = \sqrt{2E_{\rm K}/M_{\rm ej}}$, where $E_{\rm K}$ is the kinetic energy of the ejecta). These parameters are summarized in Table 1. Even with different binary parameters, the behaviors of the emission are expected to resemble each other as long as the ejecta mass and characteristic velocity are similar. We see further effects of the ejecta geometry in Section 3.

Table 1
Summary of Models Employed for the Radiative Transfer Simulations

Model (BH–NS)	$M_{\rm BH}$ ($M_\odot$)	$M_{\rm NS}$ ($M_\odot$)	$M_{\rm ej}$ ($M_\odot$)	$E_{\rm K}$ (erg)	$v_{\rm ch}$ (c)
APR4Q3a75	4.05	1.35	1×10^{-2}	5×10^{50}	0.24
H4Q3a75	4.05	1.35	5×10^{-2}	2×10^{51}	0.21
MS1Q3a75	4.05	1.35	7×10^{-2}	4×10^{51}	0.25
Model (NS–NS)	$M_{\rm NS}$ ($M_\odot$)	$M_{\rm NS}$ ($M_\odot$)	$M_{\rm ej}$ ($M_\odot$)	$E_{\rm K}$ (erg)	$v_{\rm ch}$ (c)
APR4-1215	1.2	1.5	0.9×10^{-2}	4×10^{50}	0.24
H4-1215	1.2	1.5	0.4×10^{-2}	1×10^{50}	0.21

Figure 1 shows the density distribution of the NS–NS merger model APR4-1215 (left) and the BH–NS merger model APR4Q3a75 (right). As demonstrated by Kyutoku et al. (2013), the mass ejection from BH–NS mergers can be highly asymmetric. We first remap the density distribution of the ejecta into a two-dimensional, axisymmetric model, imposing north–south symmetry. The mass ejection found in the numerical-relativity simulations is, however, not axisymmetric, but occurs in a particular direction near the equatorial plane with an opening angle of about 180 deg. To reproduce such anisotropic mass ejection, we omit this modeled, axisymmetric density structure at $x > 0$, and enhance the density at $x < 0$ by a factor of two, keeping the total ejecta mass. Even with this simplification, our model still captures the global density distribution which characterizes the BH–NS merger ejecta (bottom panels of Figure 1). The numerical-relativity simulations typically follow the dynamics of BH–NS coalescences up to about $t = 10$ ms after the merger. On the other hand, we start radiative transfer simulations from $t = 0.1$ days. For the evolution between these epochs, we simply scale down the density as $\rho \propto t^{-3}$. Note that this assumption might overestimate the density at later epochs because continuous radioactive heating is neglected (see Rosswog et al. 2013a).

2.2. Methods

For radiative transfer, we use a three-dimensional, time-dependent, multi-frequency Monte Carlo radiative transfer code developed by TH13. For a given density structure and abundance distribution, the code computes the time series of spectra in the UVOIR wavelengths. The code adopts a three-dimensional Cartesian grid, typically with 32^3 cells. Thanks to the nearly homologous expansion, velocity is used as a spatial coordinate. For the models presented in this paper, a typical spatial resolution is $\Delta v \sim 2000$ km s^{-1}. For the time grid, we use a logarithmically spaced time step, with a time step of $\Delta \log(t/{\rm day}) = 0.05$. For the frequency grid, we use a linearly spaced grid in the wavelength, λ = 100–25,000 Å with $\Delta\lambda = 10$ Å.

A major update of the code is the heating rate, for which TH13 adopted only an approximated recipe. The radioactive heating rate from *r*-process nuclei has been studied by several authors according to nucleosynthesis calculations (e.g., Metzger et al. 2010; Goriely et al. 2011; Korobkin et al. 2012; Grossman et al. 2013). Grossman et al. (2013) pointed out that the heating rate computed from their calculations was lower than that assumed

[5] See Jin et al. (2013) for an alternative scenario, involving synchrotron radiation by a wide, mildly relativistic outflow, although non-detection of late-phase radio emission does not support this scenario (Fong et al. 2013).

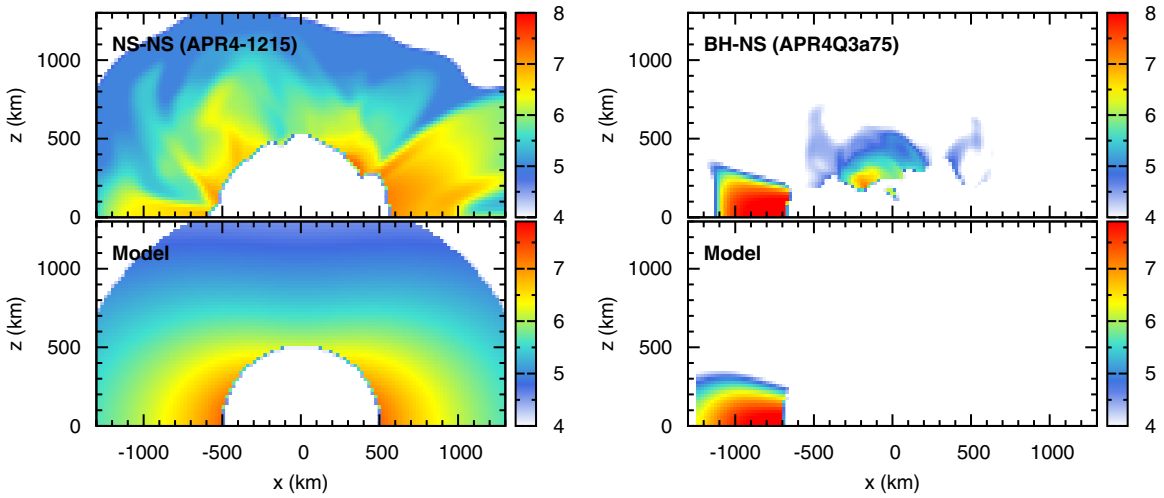

Figure 1. Density distributions of the NS–NS merger model APR4-1215 (Hotokezaka et al. 2013a; left) and the BH–NS merger model APR4Q3a75 (Kyutoku et al. 2013; right) at $t \sim 10$ ms after the merger. The top panels show the results of numerical relativity simulations while the bottom panels show the modeled, smoothed density structures, which are used as input of radiative transfer simulations. The vertical (z) axis is perpendicular to the orbital plane of the merger. The color bar indicates $\log \rho$ in g cm^{-3}. In BH–NS mergers, the mass ejection is non-axisymmetric and concentrated near the equatorial plane. Only the escaping material is shown in the plots.

(A color version of this figure is available in the online journal.)

in TH13. They also showed that the heating rate depended on the initial Y_e (number of protons per nucleon) in the ejecta. It is noted that a prediction of the r-process abundance curve is subject to uncertainties in the astrophysical models as well as in the theoretical nuclear data adopted in nucleosynthesis calculations (e.g., Metzger et al. 2010).

For demonstrative purposes, in this paper we simply assume the time-independent abundance distribution as a function of A, Y_A (number of nuclei with A per nucleon), being the same as the solar system r-process pattern (Cowan et al. 1999). Note that Y_A is the sum of the time-dependent abundances of the isobars with different atomic numbers, Z, in the neutron-rich side of β-stability. We have computed the heating rate starting from the initial compositions Y_A at the neutron separation energies of 2 MeV (roughly at the r-process freezeout; the result is almost independent of this value). Here, heating is due to β-decays that do not change A but increase Z of a given nuclide; β-delayed neutron emission (which changes A), plays a role only during the first seconds, and is not considered. After several seconds, most of the nuclei decay back to the vicinity of β-stability, where experimental half-lives (Horiguchi et al. 1996; Nishimura et al. 2011) and Q-values (from the nuclear masses compiled by G. Audi & W. Meng 2011, private communication) are available. The uncertainties originating from the theoretical nuclear data are thus irrelevant. Heating from nuclear fission (which changes A) is not considered here; this should be subdominant in our case (assuming the solar r-process pattern of Y_A) because of the abundant $A \sim 130$ nuclei that dominate the radioactive energies (Metzger et al. 2010).

Figure 2 shows the heating rates computed from the initial compositions reproducing the solar r-process abundance ratios for $A \geqslant 70$ (black), $A \geqslant 90$ (red), and $A \geqslant 120$ (blue). The results are found to be similar as long as the minimal masses $A = 90$–120 are considered. In this paper, we use the heating rate with $A \geqslant 90$, which is smaller than that adopted in TH13 by a factor of about three at $t = 1$–10 days and in good agreement with the mentioned nucleosynthetic results (Metzger et al. 2010; Goriely et al. 2011; Korobkin et al. 2012; Grossman et al. 2013).

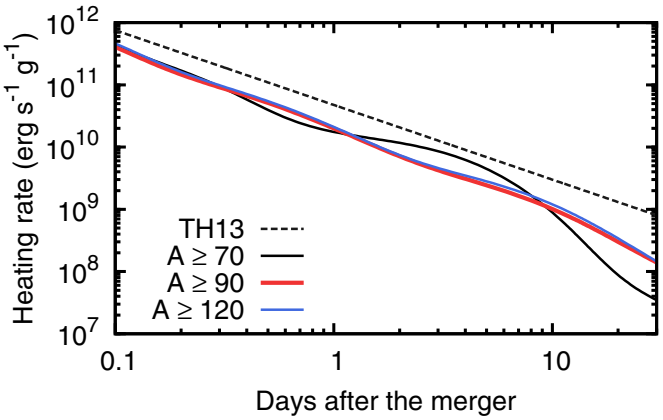

Figure 2. Heating rate from the β-decays of r-process nuclei. Black, red, and blue solid lines show the heating rates computed from the initial conditions reproducing the solar r-process abundance ratios with $A \geqslant 70$, $A \geqslant 90$, and $A \geqslant 120$, respectively. The dashed line shows the approximated heating rate adopted by TH13. In this paper, we use the heating rate with $A \geqslant 90$ (red line).

(A color version of this figure is available in the online journal.)

As in TH13, the effect of γ-ray transport is crudely taken into account by introducing a thermalization factor $\epsilon_{\rm therm}$ (Metzger et al. 2010; Korobkin et al. 2012). A fraction $\epsilon_{\rm therm}$ of the decay energy $\dot{E}_{\rm decay}$ (in Figure 2) is assumed to be thermalized, i.e., $\dot{E}_{\rm rad} = \epsilon_{\rm therm} \dot{E}_{\rm decay}$, where the energy $\dot{E}_{\rm rad}$ is immediately deposited. We adopt $\epsilon_{\rm therm} = 0.5$.

For the elemental abundances in the ejecta, we assume homogeneous distribution with the solar abundance ratios as in TH13 (i.e., detailed nucleosynthesis is not solved) both for BH–NS and NS–NS mergers. To be consistent with the assumption for the heating rate, we include elements with $Z \geqslant 40$ (Zr and heavier).

A key ingredient of the simulations is the calculation of the opacity. The wavelength-dependent opacity is computed by taking into account electron scattering, and bound–bound, bound–free, and free–free transitions. Among these opacities, the bound–bound opacity is always dominant. The code includes

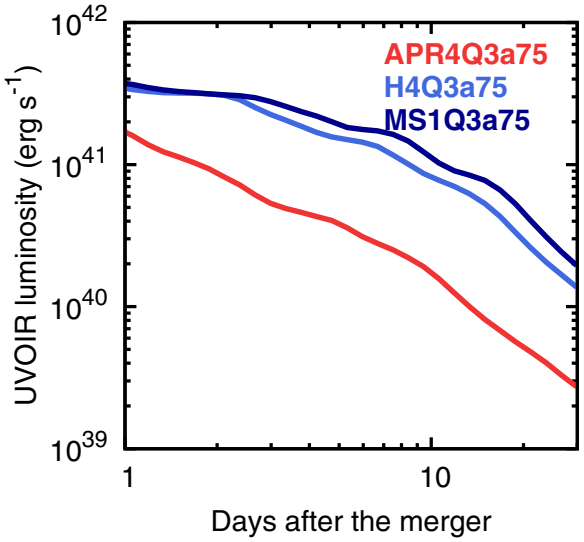

Figure 3. Bolometric light curves of the BH–NS merger models. The luminosities are those averaged over all solid angles. Different colors show the models with different EOSs adopted in the merger simulations. The BH–NS mergers with stiff EOSs (H4 and MS1) are brighter than that with a soft EOS (APR4) because of the larger ejecta mass for the stiffer EOSs.

(A color version of this figure is available in the online journal.)

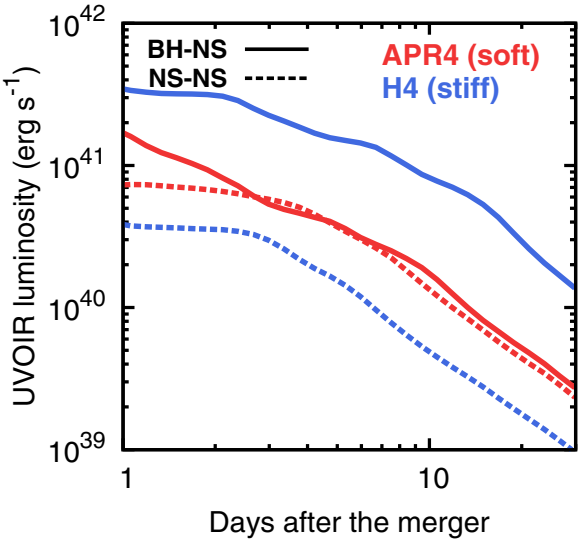

Figure 4. Bolometric light curves of the BH–NS (APR4Q3a75 and H4Q3a75, solid lines) and NS–NS merger models (APR4-1215 and H4-1215, dashed lines). The luminosities are those averaged over all solid angles. For the NS–NS merger models, the heating rate per ejecta mass is assumed to be the same with the BH–NS merger models (see the main text). A stiffer EOS (blue lines) leads to a higher luminosity by the larger ejecta mass for BH–NS mergers while it leads to a lower luminosity for NS–NS mergers.

(A color version of this figure is available in the online journal.)

the bound–bound opacities of almost all of the *r*-process elements from the VALD database (Piskunov et al. 1995; Ryabchikova et al. 1997; Kupka et al. 1999, 2000). As discussed in TH13, our line list includes the data for *r*-process elements only up to doubly ionized ions (there are no data for triply and more ionized ions in the VALD database). As a result, the code cannot correctly evaluate the opacity (and gives an extremely low opacity) at the epoch of $t \lesssim 1$ day, when the temperature is higher than about 10,000 K. To avoid this artificially low opacity, we set a lower limit to the opacity of $\kappa_{\rm low} = 1\ {\rm cm}^2\ {\rm g}^{-1}$, and assume a gray opacity of $\kappa_{\rm low}$ when the computed Rosseland mean opacity is lower than this value. For the most part in this paper, we do not discuss the emission at such early epochs which would be affected by the above assumption (see also Appendix B of TH13).

3. RESULTS

3.1. Dependence on the EOS and Comparison with NS–NS Mergers

Figure 3 shows the computed light curves of the BH–NS merger models. The luminosities are those averaged over all solid angles. Because of the ejecta entirely made of *r*-process elements, their opacities for the BH–NS mergers reach $\kappa \sim 10\ {\rm cm}^2\ {\rm g}^{-1}$ as in the NS–NS mergers (Kasen et al. 2013; Barnes & Kasen 2013; TH13).

The mass ejection in the BH–NS merger occurs dominantly by the tidal effect. When a stiffer EOS, such as H4 or MS1, is adopted, the NS radius is larger and the tidal disruption is more efficient. Thus, the ejecta mass becomes larger with a stiffer EOS for a given mass ratio and BH spin (Kyutoku et al. 2013). As a result, the models with stiffer EOSs are brighter for a given mass ratio and BH spin, provided that the heating rates are not dependent on the adopted EOSs.

The peak luminosity and the transition time to the declining phase approximately scale with $L \propto M_{\rm ej}^{1/2}$ and $t \propto M_{\rm ej}^{1/2}$, respectively, as expected by analytic formulae (Li & Paczyński 1998; Metzger et al. 2010). At declining phases, the photon diffusion is not important, and the luminosity scales with $L \propto M_{\rm ej}$ as long as a constant thermalization factor $\epsilon_{\rm therm}$ is adopted.

Figure 4 shows the bolometric light curves of the BH–NS merger models (solid lines) compared with those of the NS–NS merger models (dashed lines). For the NS–NS merger models, the gravitational masses of two NSs are $1.2\,M_\odot$ and $1.5\,M_\odot$ (Hotokezaka et al. 2013a). The light curves of these NS–NS merger models have been shown in TH13, but for ease of comparison, we show the light curves computed with the same heating rate taken for the BH–NS merger models.

For the mass ratio ($Q = 3$) and BH spin parameter ($\chi = 0.75$) adopted in our models, mass ejection from BH–NS mergers tends to be more efficient than that from NS–NS mergers. The light curves of such BH–NS merger models (solid lines) are more luminous than those of NS–NS merger models as long as the same heating rate is assumed.[6] Among the NS–NS merger models shown in TH13, the model with the APR4 EOS (red dashed line in Figure 4) gives the highest luminosity. The luminosities of the BH–NS merger models H4Q3a75 and MS1Q3a75 are higher than that of the NS–NS merger model with the APR4 EOS by a factor of ∼5. As already discussed in Kyutoku et al. (2013), the dependencies on EOSs are opposite between BH–NS and NS–NS mergers; a stiffer EOS leads to brighter light curves in BH–NS mergers while it results in fainter light curves in NS–NS mergers.

Interestingly, even with the similar ejecta mass, the behaviors of multi-band light curves can be different between BH–NS and NS–NS mergers. Figure 5 shows the multi-band light curves of the BH–NS merger model APR4Q3a75 (solid line)

[6] Since the dominant mechanism of mass ejection in NS–NS mergers can be shock heating (especially when the mass ratio of the two NSs is close to unity, Hotokezaka et al. 2013a), Y_e in the ejecta can be quite different between NS–NS and BH–NS mergers. As discussed by Grossman et al. (2013), such a difference can affect the heating rate.

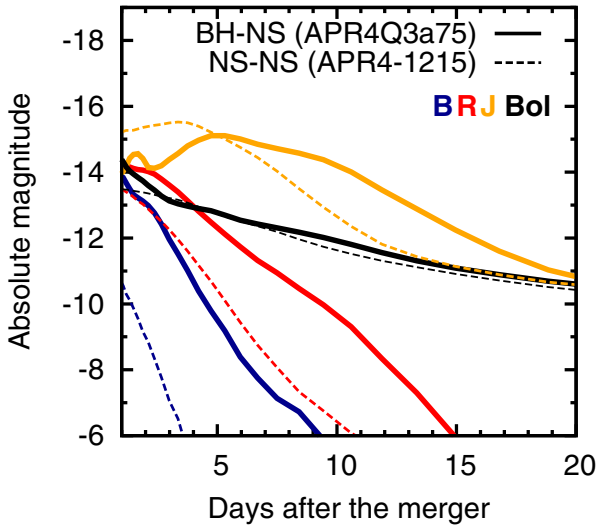

Figure 5. B, R, J-band, and bolometric light curves of the BH–NS merger model APR4Q3a75 (solid) and the NS–NS merger model APR4-1215 (dashed). Although the bolometric light curves of these two models (with similar ejecta masses, $M_{\rm ej} \sim 0.01\,M_\odot$) are similar, the light curves of the BH–NS merger model in the optical bands (B and R bands in this figure) are brighter than those of the NS–NS merger model.

(A color version of this figure is available in the online journal.)

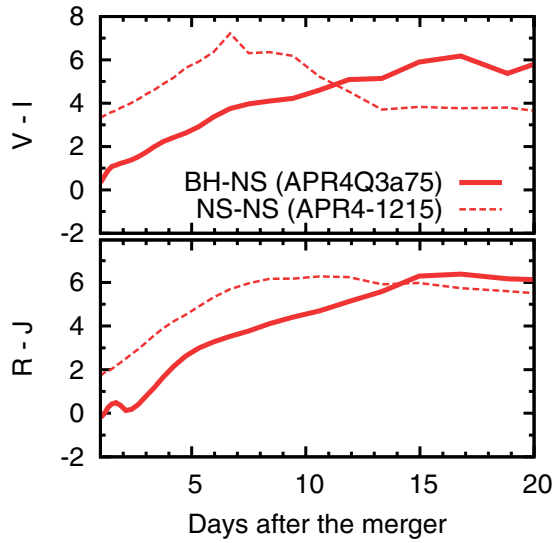

Figure 6. Color evolutions (top: $V-I$ color, bottom: $R-J$ color) of the BH–NS merger model APR4Q3a75 (solid) and the NS–NS merger model APR4-1215 (dashed). The BH–NS merger model has bluer colors in the first 10 days.

(A color version of this figure is available in the online journal.)

and the NS–NS merger model APR4-1215 (dashed line). Although these two models have similar bolometric luminosities (Figure 4),[7] the light curves of the BH–NS merger model in the optical bands (*UBVRI*) are brighter than those of the NS–NS merger model. This difference is clearly shown in the color evolutions shown in Figure 6. The $V-I$ and $R-J$ colors of the BH–NS merger are bluer than those of the NS–NS merger by 2 mag during the first 10 days.

The difference in the color evolutions mainly results from the ejecta geometries. Figure 7 shows the temperatures at

[7] The light curve of BH–NS merger model APR4Q3a75 has a slightly higher peak luminosity at earlier epochs than that of the NS–NS merger model APR4-1215. As already discussed by Kyutoku et al. (2013), this is due to a short diffusion length/timescale for the BH–NS merger ejecta.

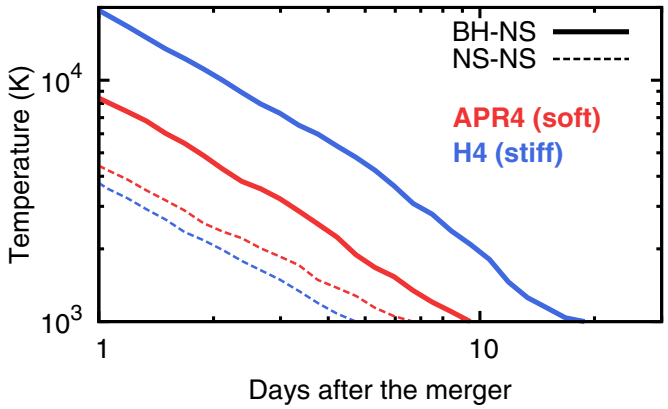

Figure 7. Temperatures of the BH–NS merger models (solid lines) and the NS–NS merger models (dashed lines) at $v = 0.25c$ (near the characteristic velocities of the models). Red and blue lines show the models with the soft (APR4) and stiff (H4) EOSs, respectively. The BH–NS merger models tend to have a higher temperature, which results in a bluer emission (Figures 5 and 6).

(A color version of this figure is available in the online journal.)

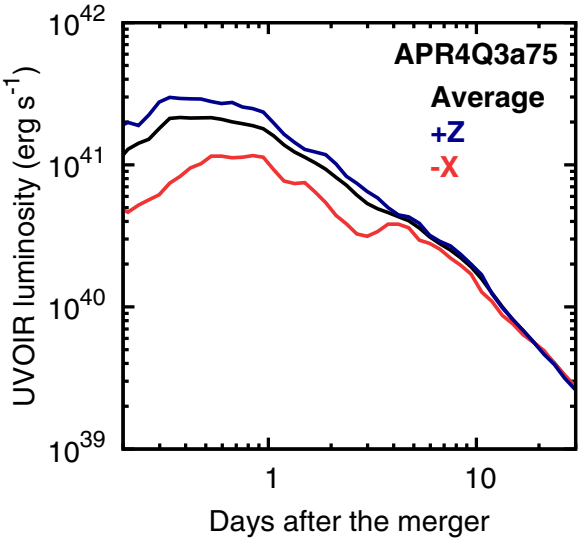

Figure 8. Bolometric light curves of the BH–NS merger model APR4Q3a75 viewed from different lines of sight (in isotropic luminosity). The light curve observed from the direction of mass ejection ($-x$ in the right panel of Figure 1) is fainter than those viewed from the other directions. Note that our simulations assume the gray opacity of $\kappa = 1\ {\rm cm^2\ g^{-1}}$ at $t \lesssim 1$ day, since our line list for bound–bound transitions is not applicable at such early epochs.

(A color version of this figure is available in the online journal.)

$v = 0.25c$, near the characteristic velocities $v_{\rm ch}$ of the models. The temperatures for the BH–NS merger models are systematically higher than those of the NS–NS merger models. It is emphasized that there is such a difference even for similar ejecta masses; the models APR4Q3a75 and APR4-1215 have similar $M_{\rm ej}$ ($\sim 10^{-2}\,M_\odot$), but their temperatures are different by a factor of about two. In the model APR4Q3a75, the mass ejection is confined in a small solid angle near the equatorial plane. Thus, for a given ejecta mass, the ejecta matter of the BH–NS merger model has a smaller volume than that of the NS–NS merger model. Since a similar radiation energy is deposited in the small volume, the temperature of the BH–NS merger model becomes higher. As a result, the emission from BH–NS merger ejecta tends to be bluer when the mass ejection is confined in a small solid angle. Implications of this trend are discussed in Section 4.

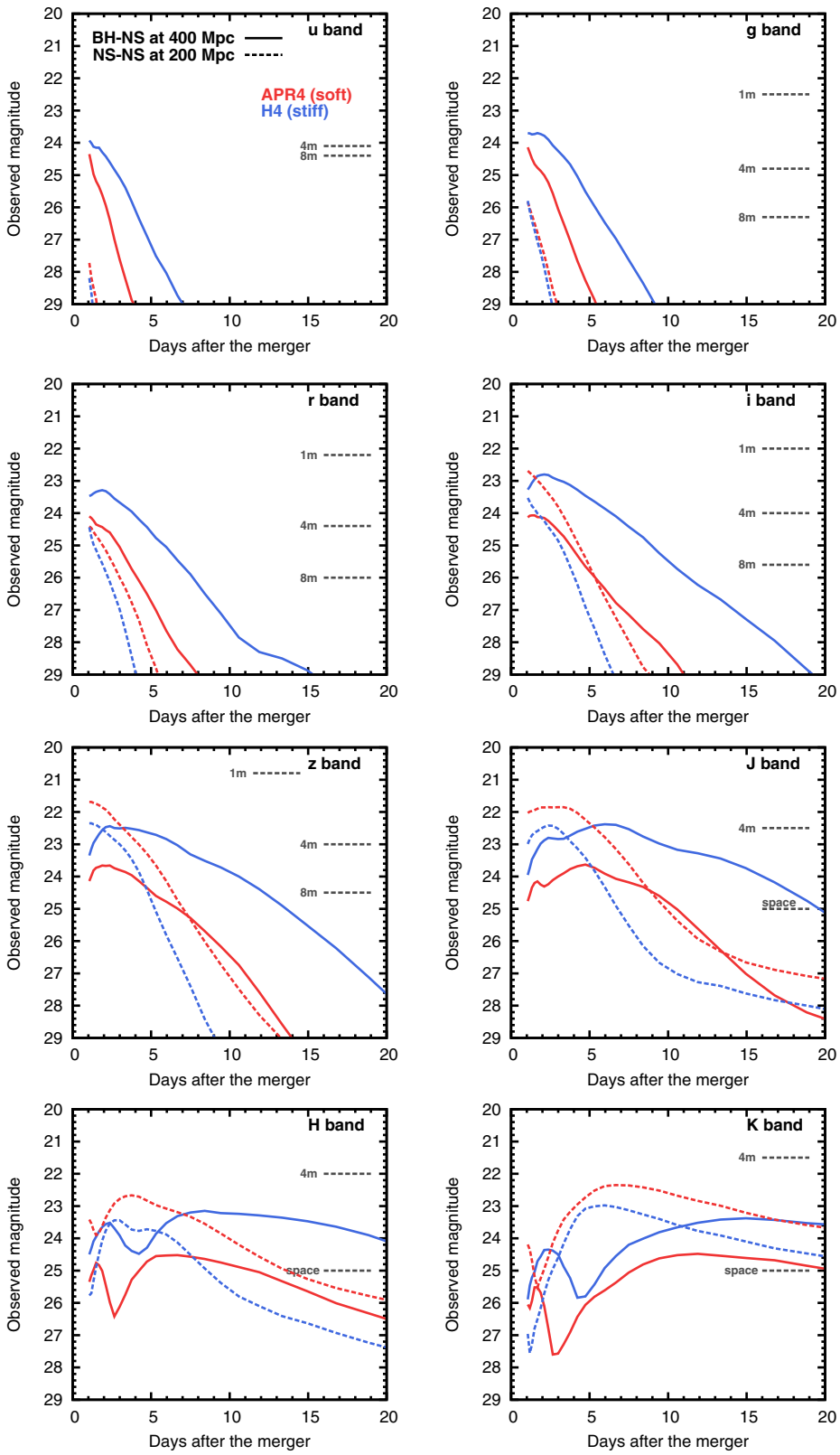

Figure 9. Expected observed *ugrizJHK*-band light curves (in AB magnitudes) for the BH–NS merger models APR4Q3a75 (red solid lines) and H4Q3a75 (blue solid lines) and the NS–NS merger models APR4-1215 (red dashed lines) and H4-1215 (blue dashed lines). The light curves are those averaged over all solid angles. The distances to the events are set to be 400 Mpc (BH–NS) and 200 Mpc (NS–NS). *K* correction is taken into account. Horizontal lines show typical limiting magnitudes for wide-field telescopes (5σ with 10 minute exposure). For optical wavelengths ($ugriz$ bands), "1 m," "4 m," and "8 m" limits are taken or deduced from those of PTF (Law et al. 2009), CFHT/Megacam, and Subaru/HSC (Miyazaki et al. 2006), respectively. For NIR wavelengths (*JHK* bands), "4 m" and "space" limits are taken or deduced from those of Vista/VIRCAM and the planned limits of WFIRST (Green et al. 2012) and WISH (Yamada et al. 2012), respectively.

(A color version of this figure is available in the online journal.)

3.2. Viewing Angle Effects

When the mass ejection from BH–NS mergers is highly asymmetric, the behaviors of the light curves are expected to depend on the line of sight of observers (Kyutoku et al. 2013). Such effects have been first studied by Roberts et al. (2011). Figure 8 shows the bolometric light curves of the model APR4Q3a75 viewed from different angles. In this plot, we include the light curves at $t < 1$ day since the viewing angle effects are most important at the earliest epochs. It should be cautioned that our simulations assume the gray opacity of $\kappa = 1$ cm^2 g^{-1} at $t \lesssim 1$ day, since our line list for bound–bound transitions is not applicable at early epochs when the temperature is $T \gtrsim 10{,}000$ K (see TH13). Nevertheless, relative behaviors of the light curves may be worth discussing.

We find that the emission viewed from the direction of mass ejection ($-x$ direction in the right panel of Figure 1) is fainter than those from the other viewing angles. This is because the diffusion path, and hence the diffusion timescale, are longer when the BH–NS merger is viewed from the direction of mass ejection. The viewing angle effect will be important only at the first five days, when the ejecta are opaque and the photon diffusion is important. Since the solid angle of mass ejection (i.e., the probability to observe BH–NS events from the direction of the mass ejection) is small, we do not expect that the viewing angle effects have a big impact on follow-up observations.

4. IMPLICATIONS FOR FOLLOW-UP OBSERVATIONS

Based on the results of our simulations, we discuss a strategy for follow-up observations of EM counterparts after the GW detection from BH–NS mergers. Figure 9 shows the expected multi-band light curves (in AB magnitudes for Sloan Digital Sky Survey *ugriz* filters and NIR *JHK* filters) for the BH–NS merger models APR4Q3a75 (red solid lines) and H4Q3a75 (blue solid lines) and the NS–NS merger models APR4-1215 (red dashed lines) and H4-1215 (blue dashed lines). Since a typical distance to BH–NS merger events is expected to be larger than that to NS–NS merger events (Abadie et al. 2010a), the distance to the BH–NS merger events is assumed to be 400 Mpc, while that to the NS–NS merger events is 200 Mpc.

For the mass ratio ($Q = 3$) and BH spin parameter ($\chi = 0.75$) aligned with the binary orbital angular momentum, the BH–NS merger models have relatively large ejecta masses. In such cases, thanks to the intrinsically higher luminosities and bluer colors, observed magnitudes of BH–NS mergers can be comparable to or even brighter than those of NS–NS mergers, compensating the larger distance. As discussed in Section 3, the dependence on the EOS is opposite for BH–NS and NS–NS mergers. The mass ejection for BH–NS mergers is more efficient with a stiff EOS (Kyutoku et al. 2013) while that for NS–NS mergers is more efficient with a soft EOS (Hotokezaka et al. 2013a; Bauswein et al. 2013). Thus, if a stiff EOS, such as H4 and MS1, is the case, radioactively powered emission from BH–NS mergers can be more easily detected than that from NS–NS mergers (see blue lines in Figure 9).

When the mass ejection for BH–NS mergers is efficient as in the models adopted in this paper, a similar follow-up strategy can be applied both for the BH–NS and NS–NS merger events. As already discussed by Barnes & Kasen (2013) and TH13, observations in the red optical and NIR wavelengths are the most efficient. In optical wavelengths, observations with wide-field 4 m and 8 m class telescopes are necessary. Such facilities include 3.6 m Canada–France–Hawaii Telescope (CFHT)/Megacam (3.6 deg^2 field of view, FOV), the Blanco 4 m telescope/DECAM (4.0 deg^2 FOV), 8.2 m Subaru/Hyper Suprime Cam (HSC; Miyazaki et al. 2006; 1.77 deg^2 FOV), and 8.4 m Large Synoptic Survey Telescope (LSST; Ivezic et al. 2008; LSST Science Collaboration 2009; 9.6 deg^2 FOV). In NIR wavelengths, observations with wide-field space telescopes, such as The Wide-Field Infrared Survey Telescope (WFIRST; Green et al. 2012; 0.375 deg^2 FOV) and Wide-field Imaging Surveyor for High-redshift (WISH; Yamada et al. 2012; 0.28 deg^2 FOV) will be important.

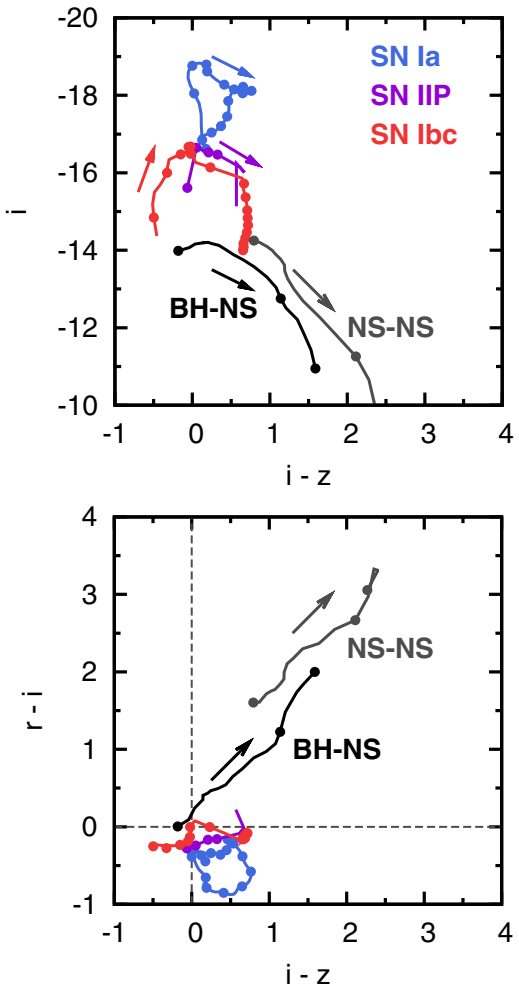

Figure 10. Color–magnitude (top) and color–color (bottom) diagrams for the BH–NS merger model APR4Q3a75 (black) and the NS–NS merger model APR4-1215 (gray). These models are compared with Type Ia (blue), IIP (purple), and Ibc (red) supernovae. The BH–NS and NS–NS mergers have fainter absolute magnitudes, and redder colors than supernovae. The arrows show the direction of time evolution, and dots for each model are shown with 5 day intervals. For supernovae, we use the spectral templates by Nugent et al. (2002). All the magnitudes are in AB magnitudes and in the rest frame (i.e., no K correction). Dashed lines in the bottom panel show the positions of $r - i = 0$ and $i - z = 0$.
(A color version of this figure is available in the online journal.)

Since BH–NS and NS–NS mergers are rare events, follow-up observations for the EM counterparts of the GW sources may discover more supernovae, which occur by chance within the localization area of GW sources.[8] Thus, classification of transient objects is extremely important. Since the timescale of

[8] Note that other variable sources, such as cataclysmic variables, high-redshift active galactic nuclei, and M-dwarf flares, will also be detected (see Nissanke et al. 2013).

the light curve evolution for BH–NS and NS–NS merger events is much faster than that for supernovae, multiple visits within 5–10 days are the most effective way to classify the transient objects as BH–NS or NS–NS merger events. However, even with observations at a single or a few epochs, a classification may be possible. Figure 10 shows the color–magnitude (top) and color–color (bottom) diagrams. These diagrams show that the radioactively powered emission from BH–NS and NS–NS mergers are fainter and redder than that from supernovae. Only at the brightest phase, the BH–NS merger models can have a similar color to that of supernovae. Thus, even without detailed light curves, we may be able to distinguish BH–NS and NS–NS mergers from supernovae with multi-band observations.

Color information can be used to effectively pick up the candidates. However, to conclusively identify the transient objects as BH–NS or NS–NS mergers, spectroscopic observations are eventually necessary. If extremely broad-line, smeared-out spectra are obtained (see Figure 6 of TH13), such an object is likely to be the counterpart of a GW source.

Interestingly, we might be able to even distinguish BH–NS mergers from NS–NS mergers by the radioactively powered emission. When the mass ejection from a BH–NS merger is confined in a small solid angle, the emission from the ejecta can have bluer colors than those for NS–NS mergers (Figures 6 and 10). In such a case, the emissions for BH–NS and NS–NS merger models occupy different regions in a color–color diagram (Figure 10). In order to find the general emission properties of BH–NS merger ejecta, we have to study a wide variety of possible models, such as models with different BH to NS mass ratios, with different BH spin parameters, and with non-aligned BH spins. Contributions from the *r*-processed ejecta from a BH-accretion torus, expected to form after the first dynamical matter ejection, should also be taken into account in the future study (Surman et al. 2008; Wanajo & Janka 2012; Fernández & Metzger 2013). Nevertheless, we emphasize that, in addition to the GW observations (see, e.g., Hannam et al. 2013), multi-band optical and NIR observations of radioactively powered emission may also provide independent information on the progenitors of GW sources (see also Hotokezaka et al. 2013b).

5. CONCLUSIONS

We have performed three-dimensional, time-dependent, multi-frequency Monte Carlo radiative transfer simulations for radioactively powered emission from BH–NS mergers by taking into account the wavelength-dependent opacities of *r*-process elements. We showed that, for the BH to NS mass ratio of $Q = 3$ and BH spin parameter of $\chi = 0.75$ aligned with the orbital angular momentum, radioactively powered emission from BH–NS mergers can be more luminous than that from NS–NS mergers. In such cases, the observed brightness of BH–NS mergers can be comparable to or even higher than that of NS–NS mergers, compensating expected typical larger distances to BH–NS mergers. Then, a similar observational strategy to identify EM counterparts works both for the BH–NS and NS–NS merger events. Observations at the red edge of optical and NIR wavelengths are most efficient. If a stiff EOS is the case, the EM counterparts of GW sources can be more easily detected for BH–NS mergers than for NS–NS mergers.

When the mass ejection from a BH–NS merger is confined in a small solid angle, a large radioactive energy is deposited to the small volume, which makes the ejecta temperature higher than that for an NS–NS merger. As a result, the emission from BH–NS mergers can be bluer than that from NS–NS mergers. Thanks to these properties, we might be able to distinguish BH–NS events from NS–NS merger events by multi-band observations of radioactively powered emission. Although the general emission properties of the BH–NS merger ejecta are still unknown, owing to, e.g., unknown mass functions and spin parameters of BHs, our results demonstrate that EM observations can potentially provide independent information on the progenitors of GW sources and the nature of compact binary coalescences.

This work was in part developed during the long-term workshop on *Gravitational Waves and Numerical Relativity* held at the Yukawa Institute for Theoretical Physics, Kyoto University in 2013 May and June. We have made use of NIST database for atomic data, and VALD database (Piskunov et al. 1995; Ryabchikova et al. 1997; Kupka et al. 1999, 2000) for line lists. Atomic data compiled in the DREAM data base (Biémont et al. 1999) were extracted via VALD. The numerical simulations presented in this paper were carried out with Cray XC30 at Center for Computational Astrophysics, National Astronomical Observatory of Japan. This research has been supported by the Grant-in-Aid for Scientific Research of the Japan Society for the Promotion of Science (JSPS, 23224004, 23740160, 24244028, 24740117, 24740163) and Grant-in-Aid for Scientific Research on Innovative Areas of the Ministry of Education, Culture, Sports, Science and Technology (MEXT, 25103510, 25103512, 25103515, 25105508). Kenta Hotokezaka is supported by JSPS fellowship Grant Number 24-1772. Koutarou Kyutoku is supported by JSPS Postdoctoral Fellowships for Research Abroad.

REFERENCES

Aasi, J., Abadie, J., Abbott, B. P., et al. 2013a, arXiv:1310.2314
Aasi, J., Abadie, J., Abbott, B. P., et al. 2013b, arXiv:1304.0670
Abadie, J., Abbott, B. P., Abbott, R., et al. 2010a, CQGra, 27, 173001
Abadie, J., Abbott, B. P., Abbott, R., et al. 2010b, NIMPA, 624, 223
Abadie, J., Abbott, B. P., Abbott, R., et al. 2012, A&A, 539, A124
Accadia, T., Acernese, F., Antonucci, F., et al. 2011, CQGra, 28, 114002
Akmal, A., Pandharipande, V. R., & Ravenhall, D. G. 1998, PhRvC, 58, 1804
Barnes, J., & Kasen, D. 2013, ApJ, 775, 18
Bauswein, A., Goriely, S., & Janka, H.-T. 2013, ApJ, 773, 78
Berger, E., Fong, W., & Chornock, R. 2013, ApJL, 774, L23
Biémont, E., Palmeri, P., & Quinet, P. 1999, Ap&SS, 269, 635
Cowan, J. J., Pfeiffer, B., Kratz, K.-L., et al. 1999, ApJ, 521, 194
Deaton, M. B., Duez, M. D., Foucart, F., et al. 2013, ApJ, 776, 47
de Ugarte Postigo, A., Thoene, C. C., Rowlinson, A., et al. 2013, arXiv:1308.2984
Eichler, D., Livio, M., Piran, T., & Schramm, D. N. 1989, Natur, 340, 126
Fernández, R., & Metzger, B. D. 2013, MNRAS, 435, 502
Fong, W.-f., Berger, E., Metzger, B. D., et al. 2013, arXiv:1309.7479
Foucart, F., Deaton, M. B., Duez, M. D., et al. 2013, PhRvD, 87, 084006
Freiburghaus, C., Rosswog, S., & Thielemann, F.-K. 1999, ApJL, 525, L121
Glendenning, N. K., & Moszkowski, S. A. 1991, PhRvL, 67, 2414
Goriely, S., Bauswein, A., & Janka, H.-T. 2011, ApJL, 738, L32
Green, J., Schechter, P., Baltay, C., et al. 2012, arXiv:1208.4012
Grossman, D., Korobkin, O., Rosswog, S., & Piran, T. 2013, arXiv:1307.2943
Hannam, M., Brown, D. A., Fairhurst, S., Fryer, C. L., & Harry, I. W. 2013, ApJL, 766, L14
Horiguchi, T., Tachibana, T., & Katakura, J. 1996, Chart of the Nuclides (Japanese Nuclear Data Committee and Nuclear Data Center, Japan Atomic Energy Research Institute)
Hotokezaka, K., Kiuchi, K., Kyutoku, K., et al. 2013a, PhRvD, 87, 024001
Hotokezaka, K., Kyutoku, K., Tanaka, M., et al. 2013b, ApJL, 778, L16
Ivezic, Z., Tyson, J. A., Acosta, E., et al. 2008, arXiv:0805.2366
Jin, Z.-P., Xu, D., Fan, Y.-Z., Wu, X.-F., & Wei, D.-M. 2013, ApJL, 775, L19
Kasen, D., Badnell, N. R., & Barnes, J. 2013, ApJ, 774, 25
Kasliwal, M. M., & Nissanke, S. 2013, arXiv:1309.1554
Kelley, L. Z., Mandel, I., & Ramirez-Ruiz, E. 2013, PhRvD, 87, 123004

Kochanek, C. S., & Piran, T. 1993, ApJL, 417, L17
Korobkin, O., Rosswog, S., Arcones, A., & Winteler, C. 2012, MNRAS, 426, 1940
Kulkarni, S. R. 2005, arXiv:astro-ph/0510256
Kupka, F., Piskunov, N., Ryabchikova, T. A., Stempels, H. C., & Weiss, W. W. 1999, A&AS, 138, 119
Kupka, F. G., Ryabchikova, T. A., Piskunov, N. E., Stempels, H. C., & Weiss, W. W. 2000, BaltA, 9, 590
Kuroda, K., & LCGT Collaboration., 2010, CQGra, 27, 084004
Kyutoku, K., Ioka, K., & Shibata, M. 2012, arXiv:1209.5747
Kyutoku, K., Ioka, K., & Shibata, M. 2013, PhRvD, 88, 041503
Kyutoku, K., Okawa, H., Shibata, M., & Taniguchi, K. 2011, PhRvD, 84, 064018
Lackey, B. D., Nayyar, M., & Owen, B. J. 2006, PhRvD, 73, 024021
Lattimer, J. M., & Schramm, D. N. 1974, ApJL, 192, L145
Lattimer, J. M., & Schramm, D. N. 1976, ApJ, 210, 549
Law, N. M., Kulkarni, S. R., Dekany, R. G., et al. 2009, PASP, 121, 1395
Lee, W. H., & Ramirez-Ruiz, E. 2007, NJPH, 9, 17
Li, L.-X., & Paczyński, B. 1998, ApJL, 507, L59
Lovelace, G., Duez, M. D., Foucart, F., et al. 2013, CQGra, 30, 135004
LSST Science Collaboration. 2009, arXiv:0912.0201
Melandri, A., Baumgartner, W. H., Burrows, D. N., et al. 2013, GCN, 14735, 1
Metzger, B. D., & Berger, E. 2012, ApJ, 746, 48
Metzger, B. D., Martínez-Pinedo, G., Darbha, S., et al. 2010, MNRAS, 406, 2650
Meyer, B. S. 1989, ApJ, 343, 254
Miyazaki, S., Komiyama, Y., Nakaya, H., et al. 2006, Proc. SPIE, 6269, 62690B
Müller, H., & Serot, B. D. 1996, NuPhA, 606, 508
Nishimura, S., Li, Z., Watanabe, H., et al. 2011, PhRvL, 106, 052502
Nissanke, S., Kasliwal, M., & Georgieva, A. 2013, ApJ, 767, 124
Nugent, P., Kim, A., & Perlmutter, S. 2002, PASP, 114, 803
Piran, T., Nakar, E., & Rosswog, S. 2013, MNRAS, 430, 2121
Piskunov, N. E., Kupka, F., Ryabchikova, T. A., Weiss, W. W., & Jeffery, C. S. 1995, A&AS, 112, 525
Roberts, L. F., Kasen, D., Lee, W. H., & Ramirez-Ruiz, E. 2011, ApJL, 736, L21
Rosswog, S. 2005, ApJ, 634, 1202
Rosswog, S., Korobkin, O., Arcones, A., & Thielemann, F.-K. 2013a, arXiv:1307.2939
Rosswog, S., Liebendörfer, M., Thielemann, F.-K., et al. 1999, A&A, 341, 499
Rosswog, S., Piran, T., & Nakar, E. 2013b, MNRAS, 430, 2585
Ryabchikova, T. A., Piskunov, N. E., Kupka, F., & Weiss, W. W. 1997, BaltA, 6, 244
Shibata, M., & Taniguchi, K. 2011, LRR, 14, 6
Surman, R., McLaughlin, G. C., Ruffert, M., Janka, H.-T., & Hix, W. R. 2008, ApJL, 679, L117
Symbalisty, E., & Schramm, D. N. 1982, ApL, 22, 143
Takami, H., Kyutoku, K., & Ioka, K. 2013, arXiv:1307.6805
Tanaka, M., & Hotokezaka, K. 2013, ApJ, 775, 113
Tanvir, N. R., Levan, A. J., Fruchter, A. S., et al. 2013, Natur, 500, 547
Wanajo, S., & Janka, H.-T. 2012, ApJ, 746, 180
Yamada, T., Iwata, I., Ando, M., et al. 2012, Proc. SPIE, 8442, 84421A